



# Tribological performance of ceramics in lubricated ultrasonic motors



Wei Qiu\*, Yosuke Mizuno, Kentaro Nakamura

Precision and Intelligence Laboratory, Tokyo Institute of Technology, 4259 Nagatsuta-cho, Midori-ku, Yokohama 226-8503, Japan

## ARTICLE INFO

### Article history:

Received 1 October 2015

Received in revised form

2 February 2016

Accepted 7 February 2016

Available online 12 February 2016

### Keywords:

Ultrasonic motors

Ceramics

Sliding friction

Lubrication

Wear mechanism

## ABSTRACT

Small ultrasonic motors are driven by the oscillation of piezoelectric transducers. They are primarily applied to equipment components that require precise movements, such as drivers for auto-focus lenses in cameras, and actuators in robots and positioning devices. While lubrication has been proven effective in improving the performance of ultrasonic motors, the friction materials still play a significant role. In this study, the suitability of four different engineering ceramics, which included alumina ( $\text{Al}_2\text{O}_3$ ), zirconia ( $\text{ZrO}_2$ ), silicon carbide ( $\text{SiC}$ ), and silicon nitride ( $\text{Si}_3\text{N}_4$ ), were investigated in the self-mated configuration. By testing the candidate materials in the actual ultrasonic motor configuration, the main wear mechanisms of these ceramics were identified under lubricated conditions, with fracture being the most dominant contributor to their wear. Among the four tested ceramics,  $\text{ZrO}_2$  was found to be the most promising material as it exhibited the mildest wear and a satisfactory level of friction. The obtained results also indicate that the fracture toughness of ceramics is more critical than their hardness. This study provides guidelines for selecting friction materials that can be used in long-lived, lubricated ultrasonic motors.

© 2016 Elsevier B.V. All rights reserved.

## 1. Introduction

Ultrasonic motors are typically driven by ultrasonic vibration of the piezoelectric transducers, which is transformed to the output force through the friction force between the rotor (or slider) and the stator. They are usually several tens of millimeters in size, and possess some advantageous properties such as high torque at low speed, high power density, quick response, and precise positioning capability [1,2]. Compared with electromagnetic motors, ultrasonic motors have superior output power because of their high power density, and no necessity of using gear systems. These advantages of ultrasonic motors enable their application as driving solutions in cameras (as drivers for auto-focus lenses), robots, and positioning devices. However, the resulting friction loss and wear of friction materials (the materials used for the contact between the rotor (or slider) and the stator) lead to low motor efficiency and short lifetime, significantly limiting their actual implementation in these fields and restricting their potential application in others.

The friction loss generation can be explained by examining one particular type of ultrasonic motors, i.e., hybrid transducer-type ultrasonic motors (HTUSMs). In these motors, torsional-longitudinal Langevin transducers are used as stators, and they consist of torsional lead zirconate titanate (PZT) disks (polarized in the circumferential direction) and longitudinal PZT disks (polarized in the thickness direction), as shown in Fig. 1. A preload is applied to a rotor

by a coil spring, thus pressing the rotor against the stator. In a HTUSM, the torsional vibrator generates the output force while the longitudinal vibrator controls the friction force (Fig. 1). When the torsional vibrator moves toward the right, the longitudinal vibrator extends to contact the rotor, transmitting the driving force through the friction force between the rotor and the stator. The displacement of the longitudinal vibrator reaches a maximum to provide the highest stress when the torsional vibrator has the largest rightward velocity; thus, a 90-degree phase difference is required between the torsional and longitudinal vibrations to drive the motor. In contrast, when the torsional vibrator moves to the left, the longitudinal vibrator shrinks to separate the rotor and the stator. Thus, the rotor can be rotated in one direction because of inertia. However, this ideal operating principle is unlikely to be realized if high preloading is applied to generate sufficient torque. The rotor and the stator cannot be detached during the negative half cycle of the torsional vibration, characterized by considerable friction loss and wear of the friction materials, which is a major reason for the low efficiency of ultrasonic motors; this issue has been extensively analyzed by Nakamura and co-workers [3–5].

To date, lubrication has not been utilized in commercial ultrasonic motors because an induced slip may lead to a significant loss of the output torque and thus a decrease in motor efficiency. However, the preload and the slip between the two sliding surfaces change instantaneously during the operation of ultrasonic motors because of the alternating vibrations in the loading and driving directions; these instantaneous changes

\* Corresponding author. Tel.: +81 45 924 5052; fax: +81 45 924 5091.

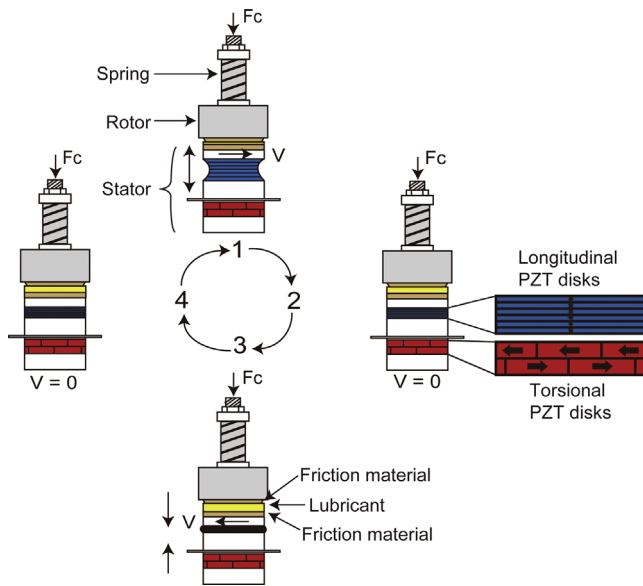


Fig. 1. Principle of operation for a hybrid transducer-type ultrasonic motor.

indicate that different lubrication regimes are likely to be implemented during one cycle of vibration. According to the theory behind the Stribeck curve [6], the friction coefficient becomes high either when a small slip occurs between the rotor and the stator, or at a high preload; both scenarios correspond to the boundary lubrication regime, during which large output forces can be achieved. In contrast, the friction coefficient decreases at large slips or low preloads, corresponding to the hydrodynamic lubrication regime, during which friction losses can be reduced. Based on this assumption, lubrication was applied to HTUSMs in our earlier studies, and it resulted in drastic improvement in the motor performance under high apparent contact pressure [5,7].

Friction materials are key components in ultrasonic motors that greatly affect their performance. More importantly, since the other major components including piezoelectric materials are generally more durable than friction materials, the lifetime of ultrasonic motors is mainly determined by the friction materials. Studies on friction materials in dry contact for ultrasonic motors cover a wide range of categories, with a particular emphasis on ceramics [8–12] and polymers [1,13–15]. Although some criteria for selecting friction materials for ultrasonic motors have been established [16,17], the tribological performance of friction materials for lubricated ultrasonic motors has yet to be investigated and may significantly differ from that under dry conditions owing to the presence of lubricants.

In this study, we used four types of advanced engineering ceramics as friction materials for lubricated ultrasonic motors. Compared with polymers, advanced engineering ceramics are characterized by high wear resistance and chemical inertness, which are desirable properties for ultrasonic motors with lubrication. The goal of this study is to select reliable friction materials for lubricated ultrasonic motors by investigating the tribological properties, especially the primary wear mechanisms, of ceramics in motors.

## 2. Materials and methods

### 2.1. Materials

Alumina ( $\text{Al}_2\text{O}_3$ , 99.5%), zirconia ( $\text{ZrO}_2$ , 94.0%), silicon carbide ( $\text{SiC}$ , 99.9%), and silicon nitride ( $\text{Si}_3\text{N}_4$ , 99.8%) ceramics were tested

**Table 1**  
Physical properties and surface roughness of the ceramics tested in this experiment.

Material property	$\text{Al}_2\text{O}_3$	$\text{ZrO}_2$	$\text{SiC}$	$\text{Si}_3\text{N}_4$
Vickers hardness (GPa)	19.1	14.7	30.5	16.1
Fracture toughness ( $\text{MPa m}^{1/2}$ )	4	6	3	5
Young's modulus (GPa)	390	200	410	290
Poisson's ratio	0.24	0.32	0.16	0.28
Bulk density ( $\times 10^3 \text{ kg/m}^3$ )	3.9	6.0	3.1	3.2
Thermal conductivity at 20 °C (W/mK)	30	3	170	26
Grain size ( $\mu\text{m}$ )	4.9	0.4	2.9	1.3
Average surface roughness $R_a$ ( $\mu\text{m}$ )	0.12	0.12	0.11	0.11
Kernel roughness depth $R_k$ ( $\mu\text{m}$ )	0.15	0.39	0.35	0.33

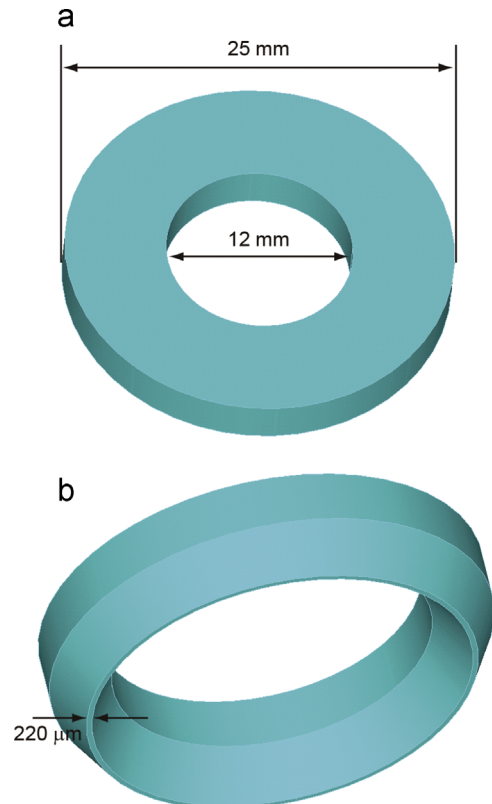


Fig. 2. Ceramic dimensions of the (a) stator and (b) rotor sides.

in this study; their physical material properties are summarized in Table 1. All four ceramic materials were sintered at high temperature, and they all possessed crystalline structures. The ceramic dimensions for the stator and rotor sides are depicted in Fig. 2; the contact width on the rotor side was  $\sim 220 \mu\text{m}$ . The same ceramics were used for both the stator and the rotor (this is known as the self-mated configuration) during each test. The Vickers hardness of each ceramic was measured at a load of 4.9 N with a Vickers hardness testing machine (HM-102, Mitutoyo Corporation, Kawasaki, Japan).

After sintering, the  $\text{Al}_2\text{O}_3$  surface was lapped using a slurry with diamond powder, while the other ceramic surfaces were ground with sharpening stones containing diamond particles ( $40 \mu\text{m}$  in diameter). The average surface roughness  $R_a$  was measured with a surface profilometer (Dektak 150, Veeco Instruments, Inc., Plainview, NY), and very similar  $R_a$  values (0.11–0.12  $\mu\text{m}$ ) were obtained for all ceramic types. In addition, the kernel roughness depth  $R_k$  (used to eliminate the effect of isolated peaks and valleys) was also calculated from the Abbott–Firestone curve by following the

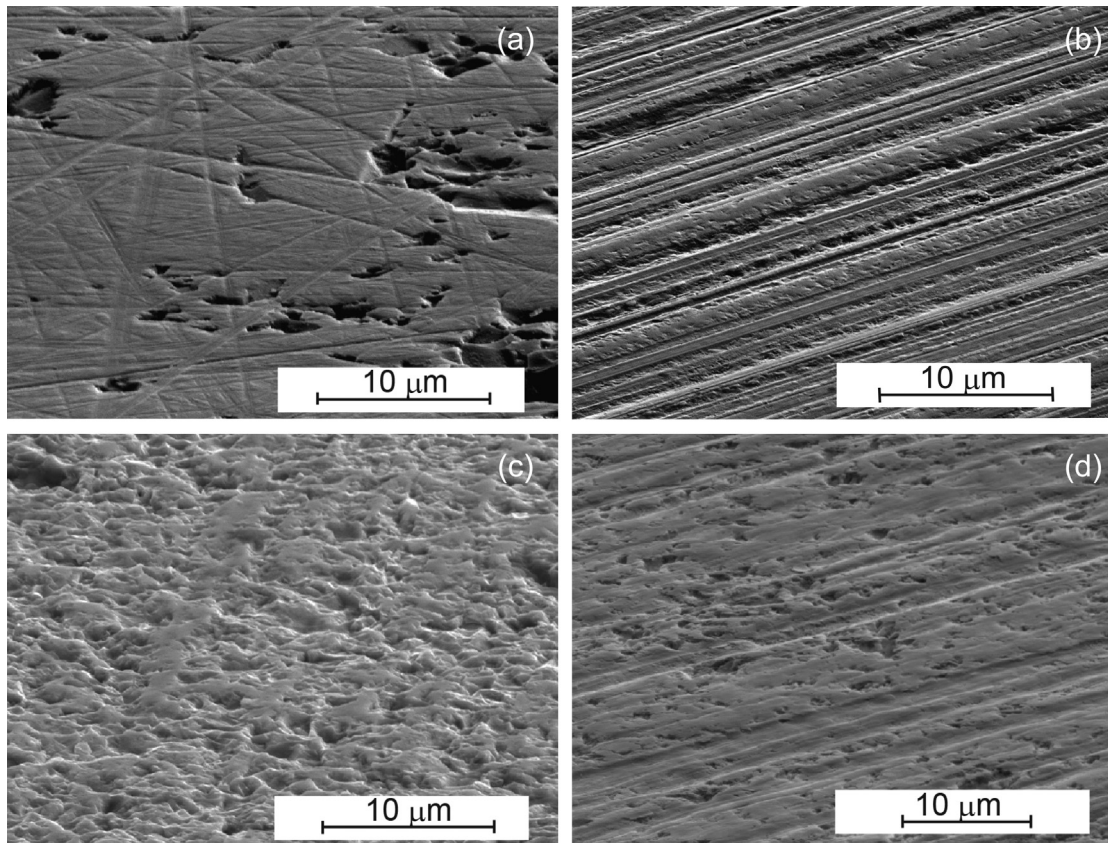


Fig. 3. Scanning electron micrographs of the unworn surfaces of the (a)  $\text{Al}_2\text{O}_3$ , (b)  $\text{ZrO}_2$ , (c)  $\text{SiC}$ , and (d)  $\text{Si}_3\text{N}_4$  ceramics. The sample tilt was equal to  $70^\circ$ .

procedures reported by Erickson et al. [18]. Comparable  $R_k$  values were obtained for the  $\text{ZrO}_2$ ,  $\text{SiC}$ , and  $\text{Si}_3\text{N}_4$  surfaces, while the value for  $\text{Al}_2\text{O}_3$  was much lower ( $0.15\ \mu\text{m}$ ), indicating that the  $\text{Al}_2\text{O}_3$  surface was smoother than surfaces of the other ceramics. The scanning electron micrographs of the unworn surfaces of the tested ceramics are shown in Fig. 3(a)–(d), confirming that the  $\text{Al}_2\text{O}_3$  surface had a smoother appearance than those of the other ceramics, corresponding to the smaller  $R_k$  value. In addition, polishing traces were observed on the  $\text{Al}_2\text{O}_3$  surface in random directions, while unidirectional traces appeared on the  $\text{ZrO}_2$ ,  $\text{SiC}$ , and  $\text{Si}_3\text{N}_4$  surfaces owing to the different polishing methods. The other material property values listed in Table 1 were obtained from the supplier.

A high-traction fluid (base oil: synthetic naphthene; additives: zinc dithiophosphate (ZDDP), calcium phenate, and organophosphates) with a viscosity of 100 cSt at  $40^\circ\text{C}$  was selected as a lubricant, which was applied every 2 h to the interface between the stator and the rotor to maintain sufficient lubrication.

In this work, we utilized HTUSMs to investigate the tribological behavior of ceramics in lubricated contact. A torsional–longitudinal Langevin transducer with a diameter of 25 mm was used as the stator in the HTUSM, in which two 4-mm-thick torsional PZT disks and six 1-mm-thick longitudinal PZT disks were clamped together using metal parts, as shown in Fig. 1.

## 2.2. Testing procedure

The experiments were conducted at room temperature ( $20^\circ\text{C}$ ). A 460 N preload (corresponding to an apparent contact pressure of 30.8 MPa) was applied to the HTUSM, which exhibited high motor efficiency [5]. The motor was driven at a frequency of  $\sim 23\ \text{kHz}$ , which was close to the resonant frequencies of the torsional and longitudinal vibrators. The voltage applied to the longitudinal

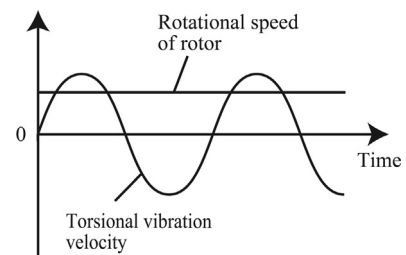


Fig. 4. Graph illustrating the change in sliding velocity of an ultrasonic motor.

vibrator was maintained at  $160\ V_{\text{rms}}$ . The amplitude of the torsional vibration velocity was fixed at  $\sim 9.0\ \text{rad/s}$ , resulting in a rotational speed of one revolution (rev) per second (1 rev/s or 1 rps) for the rotor. In general, the sliding speed of an ultrasonic motor varies because of the alternating vibration (Fig. 4): its value is low during the driving period (when the torsional vibration velocity exceeds the rotational speed of the rotor), and it becomes high when the stator moves in the direction opposite to that of the rotor. A high preload and a relatively low rotational speed were selected in our experiments because ultrasonic motors are generally employed in high-torque applications with low speeds. Each test was run for 100 h, corresponding to 360,000 motor rev and a total sliding distance of 24.31 km.

Owing to the difficulty in measuring the friction force during motor operation, the friction coefficient was estimated from the falling curve of the motor rotational speed when the input power was switched off [19]. In dry contact, the rotational speed of an ultrasonic motor decreases linearly after the power is switched off. The retarding torque of ultrasonic motors  $T_R$  (the torque without

ultrasonic vibration) can be calculated as

$$T_R = J \frac{d\Omega}{dt} = J \frac{\Omega_0}{t_f},$$

where  $J$ ,  $\Omega$ ,  $\Omega_0$ , and  $t_f$  represent the moment of inertia, rotational speed, no-load speed, and fall time (the time lapse from the highest speed (no-load) to zero speed), respectively. Meanwhile,  $T_R$  can also be expressed as

$$T_R = \mu Fr,$$

where  $\mu$ ,  $F$ , and  $r$  represent the friction coefficient, preload, and contact radius, respectively. Hence, the friction coefficient without ultrasonic vibration  $\mu$  can be obtained from

$$\mu = \frac{J\Omega_0}{t_f Fr}.$$

According to the Stribeck curve,  $\mu$  depends on the relative velocity of the contacting surfaces under lubrication. The boundary lubrication regime is activated at high preloads and low rotational speeds, especially under pure sliding conditions between two parallel surfaces, which was the case in these experiments. After the power was switched off, the sliding speed decreased from 68 mm/s (at a rotational speed of 1 rps) to 0 under a 460 N preload. The obtained falling curves of the rotational speed were characterized by linear profiles, indicating that the  $\mu$  value was constant, and the boundary lubrication regime was initiated during deceleration.

Friction measurements were performed after the motor ran for 1,000; 10,000; 50,000; 100,000; 150,000; 200,000; 250,000; 300,000; and 350,000 rev. After the wear test, the worn surfaces of both the stator and the rotor sides were studied using scanning electron microscopy (SEM). Chemical compositions of the worn surfaces were also analyzed by energy-dispersive X-ray spectroscopy (EDS).

### 3. Results

The worn  $\text{Al}_2\text{O}_3$  surfaces on the rotor and stator sides are illustrated in Fig. 5(a)–(c). On the rotor side,  $\text{Al}_2\text{O}_3$  grains were removed from the lower layer of the surface where microfractures were observed. No signs of wear debris agglomeration were detected on the surface, suggesting that the wear debris was transported from the contact area or directly dissolved by the lubricant. Similar morphology was observed in a small fraction of the worn  $\text{Al}_2\text{O}_3$  surface on the stator side (Fig. 5(b)). However, the majority of the surface was characterized by extremely mild wear and traces left from the initial polishing, as shown in Fig. 5(c). The worn surface profile for the stator side was also examined (Fig. 6(a)). Since the surface area on the rotor side was smaller than that on the stator side, a groove should appear on the stator side if the wear volume was large. However, no distinct grooves were observed on the worn  $\text{Al}_2\text{O}_3$  surface, indicating that its wear was relatively mild. The obtained EDS results showed the presence of elemental P, Zn, and Ca from the lubricant on the worn  $\text{Al}_2\text{O}_3$  surfaces (Table 2).

The worn  $\text{ZrO}_2$  surfaces on both the stator and rotor sides were characterized by extremely mild wear, with no distinct differences between the unworn and worn surfaces (Fig. 7(a) and (b)). The initial polishing traces were clearly visible, while no grooves were observed on the worn surface on the stator side (Fig. 6(b)). Only elemental Zn from the lubricant was detected on the worn  $\text{ZrO}_2$  surfaces.

The worn SiC surface on the rotor side, shown in Fig. 8(a)–(c), exhibited two types of surface morphology, where both microfractures and smooth regions were observed in a large area. Surface fractures were detected on most of the middle part, with small areas of smooth surfaces nearby along the two sides of the wear scar (Fig. 8(a) and (b)). In addition, some areas of the worn surface were mostly

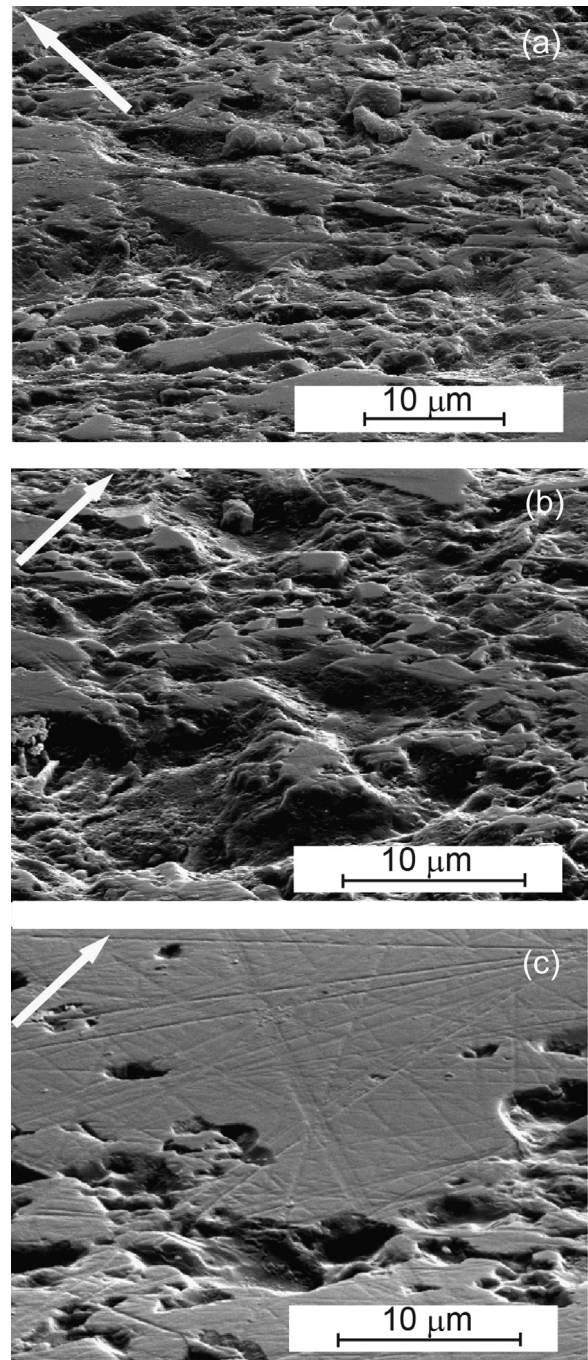
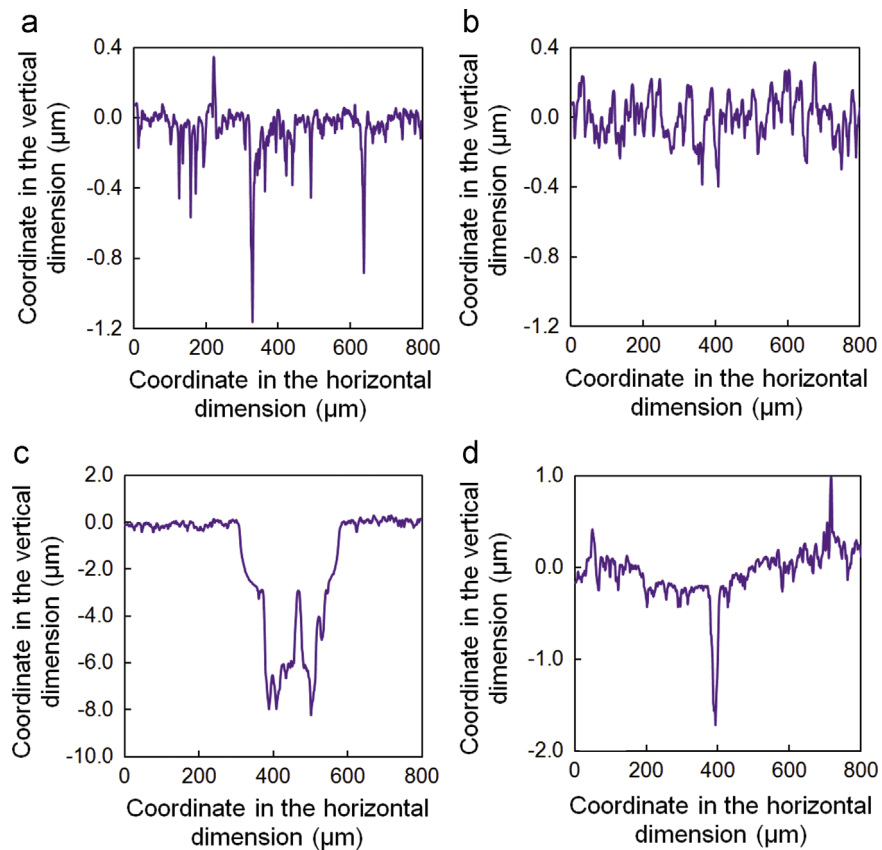


Fig. 5. (a) Scanning electron micrograph of the worn  $\text{Al}_2\text{O}_3$  surface on the rotor side. Scanning electron micrographs showing (b) the fractured region and (c) the mild wear region on the worn  $\text{Al}_2\text{O}_3$  surface on the stator side. The sample tilt was equal to 70°. The arrows indicate the sliding directions.

covered by a smooth layer containing agglomerations of the wear debris (Fig. 8(c)). The debris layer was found to be strongly attached to the wear track since it could not be removed by ultrasonic cleaning. The surface appearance on the stator side was slightly different, exhibiting very mild wear in a very small region of the surface. The  $R_k$  values for the fractured and smooth regions on the stator side were 5.24 and 0.08  $\mu\text{m}$ , respectively. No elements from the lubricant were detected on the worn SiC surface, while the related O content slightly increased.

Most of the outer grains of the worn  $\text{Si}_3\text{N}_4$  surface on the stator side were polished and covered by a thin surface layer, although some initial polishing traces could still be observed (Fig. 9(a)). The



**Fig. 6.** Worn surface profiles of the (a)  $\text{Al}_2\text{O}_3$ , (b)  $\text{ZrO}_2$ , (c)  $\text{SiC}$  (fractured region), and (d)  $\text{Si}_3\text{N}_4$  (polished region) ceramics on the stator side.

**Table 2**

Chemical composition of the unworn and worn surfaces of four different ceramics obtained by EDS.

Material	Detected elements	
	Unworn surface	Worn surface
$\text{Al}_2\text{O}_3$	Al, O	Al, O, P, Zn, Ca
$\text{ZrO}_2$	Zr, O, Y	Zr, O, Y, Zn
$\text{SiC}$	Si, C, O	Si, C, O
$\text{Si}_3\text{N}_4$	N, O, Si, Al, Y	N, O, Si, Al, Y, Zn, Ca

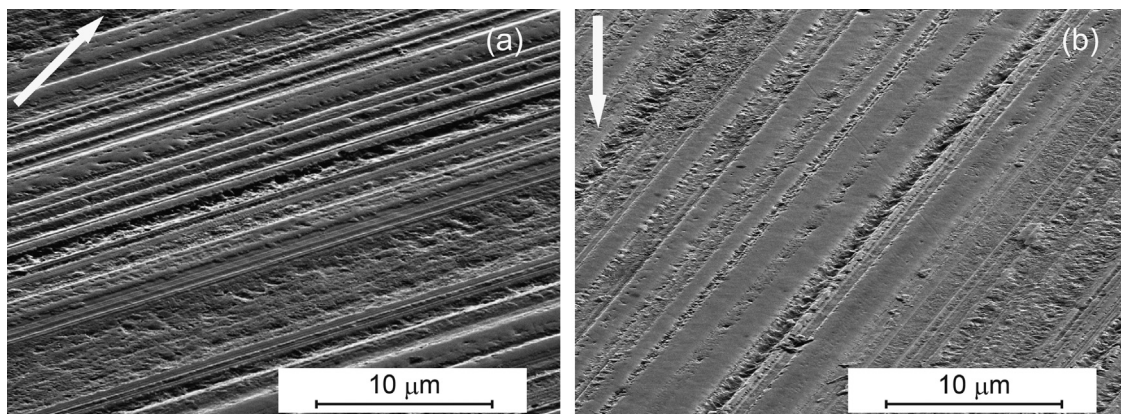


**Fig. 7.** Scanning electron micrographs of the worn  $\text{ZrO}_2$  surface on the (a) stator side and (b) rotor side. The sample tilt was equal to  $70^\circ$ . The arrows indicate the sliding directions.

obtained  $R_k$  value was  $0.21 \mu\text{m}$ , which is slightly lower than that for the unworn surface. In addition, several grooves indicating more severe plastic deformation were detected in some regions of the

worn surface, from which the initial surface layer was completely removed (Fig. 9(b)), resulting in the  $R_k$  value of  $0.82 \mu\text{m}$ . The worn  $\text{Si}_3\text{N}_4$  surface on the rotor side exhibited a similar appearance, while

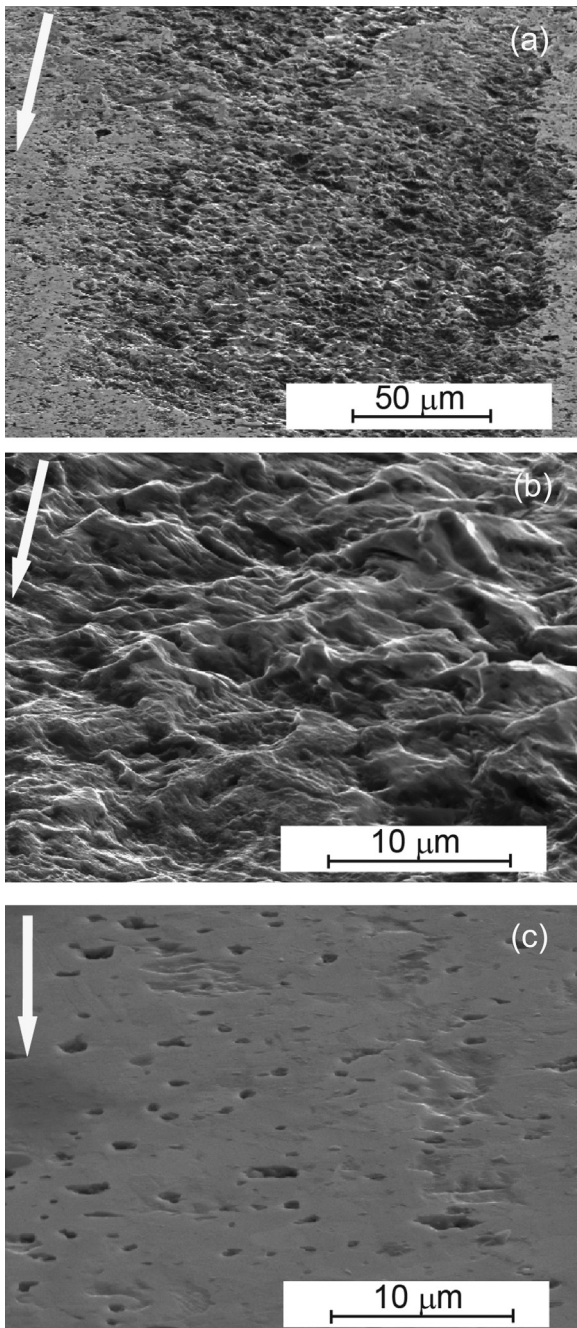


**Fig. 8.** (a) Scanning electron micrograph of the worn SiC surface with both fractured and smooth morphologies on the rotor side. Magnified views of the area inside the (b) fractured region and (c) smooth region. The sample tilt was equal to 70°. The arrows indicate the sliding directions.

more grooves were formed along the sliding direction and they were much longer than those on the stator side (Fig. 9(c)). Elemental Zn and Ca from the lubricant were detected on the worn  $\text{Si}_3\text{N}_4$  surfaces, and the related O content increased.

The dependence of the friction coefficient on the number of revolutions is shown in Fig. 10. The plotted data represent averaged values of 10 measurements. The friction forces of the motors with the SiC and  $\text{Si}_3\text{N}_4$  ceramics were relatively stable, leading to small changes in their friction coefficients (ranging from 0.13 to 0.15). In contrast, the friction coefficients of the  $\text{Al}_2\text{O}_3$  and  $\text{ZrO}_2$  ceramics increased after initial operation and then stabilized after 50,000 rev (0.17–0.19 for  $\text{Al}_2\text{O}_3$ ; 0.19–0.21 for  $\text{ZrO}_2$ ) until they finally decreased to levels similar to those of the SiC and  $\text{Si}_3\text{N}_4$  ceramics after 250,000 rev.

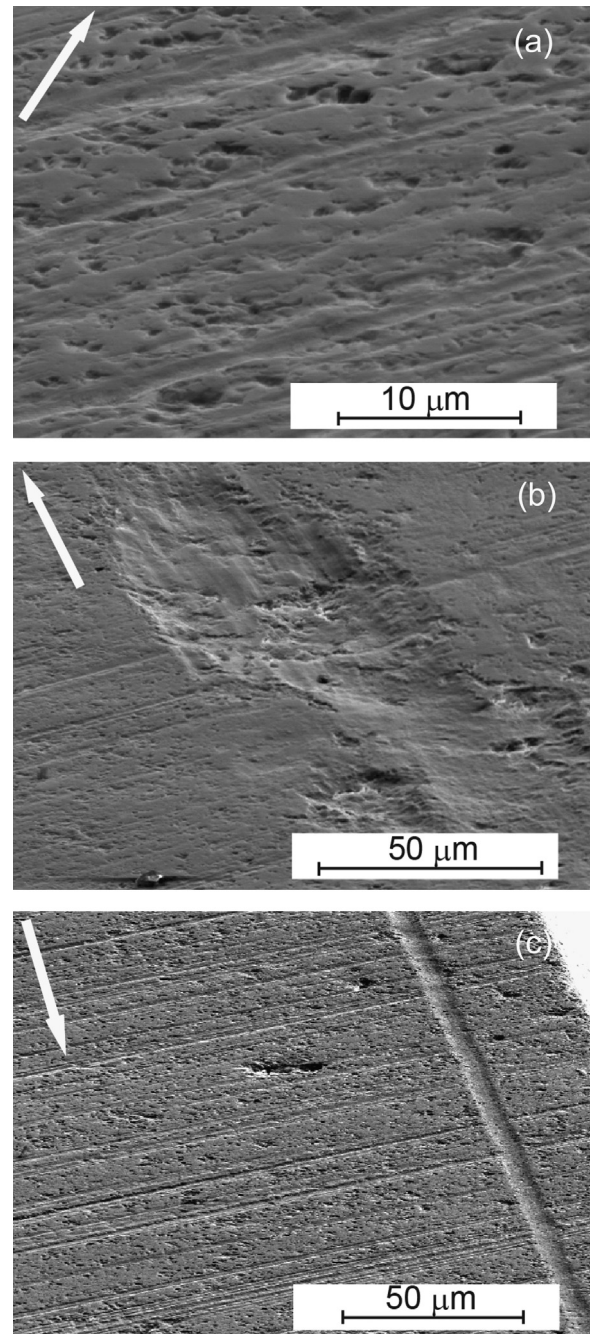


**Fig. 9.** Scanning electron micrographs of the worn  $\text{Si}_3\text{N}_4$  surface: (a) mild wear region; (b) region with a groove on the stator side; (c) region with a groove on the rotor side. The sample tilt was equal to 70°. The arrows indicate the sliding directions.

#### 4. Discussion

The worn surfaces of three ceramic types (all but  $\text{ZrO}_2$ ) on the stator and rotor sides were characterized by different appearances, possibly because the stressed volume on the stator side was confined by the surrounding unstressed material during motor operation as a result of the difference in material shapes. The worn  $\text{Al}_2\text{O}_3$ , SiC, and  $\text{Si}_3\text{N}_4$  surfaces exhibited both mild and severe wear regions, probably because of the non-uniform preloads produced by the coil spring. In general, uniform preloads are not required for HTUSMs since their mechanical characteristics are not significantly affected by the uniformity of preloads (in contrast to surface acoustic wave motors [20]). However, non-uniform preloads caused high stresses in some areas on

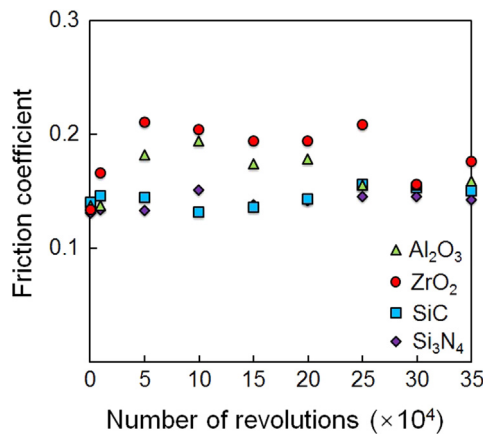


Fig. 10. Measured dependence of the friction coefficient on the number of revolutions for various ceramic materials.

the stator side, resulting in the formation of regions characterized by severe wear.

The ZrO<sub>2</sub> ceramic exhibited the mildest wear (compared to the other tested ceramics), and the worn and unworn surfaces were almost indistinguishable because ZrO<sub>2</sub> had the highest fracture toughness among the four ceramics. In addition, according to the wear map of ZrO<sub>2</sub>, severe wear usually occurs either at high sliding speeds or high temperatures [21,22]. In a HTUSM, high sliding speeds arise only during the negative half cycle of the torsional vibration, corresponding to a low dynamic preload due to the longitudinal vibration, while the presence of the lubricant reduces the interfacial temperature. Moreover, the friction coefficient of ZrO<sub>2</sub> after lubrication was maintained within an appropriate range (0.15–0.2) in our study: the initial value of the friction coefficient was 0.13; it increased to 0.2 after 50,000 rev and finally decreased to 0.15 after 300,000 rev. At the present time, we do not have any experimental data to explain such complex behavior. However, since the surface topography was not significantly changed, the variation in friction coefficient was due to neither the change in contact pressure nor the tribochemical reaction.

The unworn Al<sub>2</sub>O<sub>3</sub> surface was the smoothest one among the tested ceramics because of the unique polishing method used for Al<sub>2</sub>O<sub>3</sub>, which was beneficial for achieving complete hydrodynamic lubrication that reduced friction loss and wear when the stator moved in the direction opposite to that of the rotor movement. Hence, the wear on the stator side was mild except for the microfractures observed in small areas. However, the fracture toughness of Al<sub>2</sub>O<sub>3</sub> was relatively low, and the stress on the rotor side was not adequately confined by the surrounding material, resulting in the development of more intensive surface microfractures. The friction coefficient was initially 0.14; it then increased to 0.19 after 100,000 rev, and finally decreased to 0.15 after 250,000 rev, showing a trend similar to that for ZrO<sub>2</sub>. The initial increase in friction coefficient was caused by the microfractures, which enhanced the local pressure of the contact asperities.

SiC exhibited the most severe wear among the tested ceramics on both the rotor and stator sides, which was mainly due to its low fracture toughness (although the hardness of SiC was the highest). The SiC wear mechanism is similar to that for the transition zone shown in the SiC wear transition diagram where microfractures are dominant [23]. The friction coefficient obtained for SiC in our study was highly stable, indicating that no chemical reaction products were formed. Tribo-oxidation may have occurred, but it is believed to have a minor influence on friction and wear since the temperature rise due to the friction heating was not significant under lubricated conditions. Although the worn surface was flattened in some areas (especially around the edges of the contact area), most of it became much

rougher ( $R_k=5.24\ \mu\text{m}$ ), indicating that hydrodynamic lubrication was not realized even after the dynamic preload reached its minimum. The stable friction coefficient indicates that severe wear was generated within a short time. No elements from the lubricant were detected on the worn surfaces, which indicate that the tribochemical reaction did not occur.

Several grooves were obtained on the worn Si<sub>3</sub>N<sub>4</sub> surfaces on both the stator and rotor sides because the wear debris was dragged along the surfaces during sliding and grooves were formed, as described in an earlier study [24]. Thus, the wear debris of Si<sub>3</sub>N<sub>4</sub> could not be easily removed from the contact zone and induced more severe wear on the surfaces, which does not satisfy the requirements as a friction material for ultrasonic motors [16]. The tribochemical reaction probably occurred because of the increased O content and the presence of elemental Zn and Ca on the worn surface.

## 5. Conclusions

Friction materials are essential components in ultrasonic motors in both dry and lubricated contact, which greatly affect the motor performance and lifetime. The tribological behavior of four types of advanced engineering ceramics was investigated for an actual ultrasonic motor lubricated with a high-traction fluid. The following major conclusions were obtained from the experimental results:

- (1) The main wear mechanism can be described by mechanical fracture of the tested ceramics in lubricated ultrasonic motors.
- (2) The ZrO<sub>2</sub> ceramic exhibited the mildest wear among the tested ceramics, indicating that ceramics possessing high fracture toughness are more suitable for lubricated ultrasonic motors. In contrast, since the SiC ceramic exhibited the most severe wear, it indicates that ceramic hardness plays a less important role than fracture toughness.
- (3) The Al<sub>2</sub>O<sub>3</sub>, SiC, and Si<sub>3</sub>N<sub>4</sub> ceramic surfaces on the rotor side experienced more severe wear than those on the stator side. Non-uniform preloading induced by a coil spring was one of the reasons for different surface morphologies on the stator side.
- (4) Smooth surfaces facilitate hydrodynamic lubrication that reduces friction loss and wear and hence improves the long-term performance of a motor, provided that the friction coefficient is maintained at an appropriate level (0.15–0.2).

We anticipate that the obtained results will provide adequate information for selecting appropriate friction materials for lubricated ultrasonic motors in the future.

## Acknowledgments

This work was supported by the Japan Society for the Promotion of Science (JSPS) KAKENHI Grant 15K13896. The work of W. Qiu was supported by a Grant-in-Aid for JSPS Research Fellows (No. 26011842). The authors are indebted to Prof. Koshi Adachi (Division of Mechanical Engineering, Tohoku University) and Dr. Satoshi Momozono (Department of Mechanical and Aerospace Engineering, Tokyo Institute of Technology) for their insightful discussions, Dr. Tso-Fu Mark Chang, Dr. Takashi Nagoshi, and Dr. Masaki Tahara (Precision and Intelligence Laboratory, Tokyo Institute of Technology) for their assistance in SEM and EDX analyses and Vickers hardness test, and Dr. Kunio Nishioka (Semiconductor and MEMS Processing Center, Technical Department, Tokyo Institute of Technology) for his assistance in the measurements of surface profiles. They also appreciate Idemitsu Kosan Co., Ltd., for providing the lubricant and the staff members of the Precision and Manufacturing Center

(Technical Department, Tokyo Institute of Technology) for machining the metal components of the motors used in the experiment.

## References

- [1] S. Ueha, Y. Tomikawa, *Ultrasonic Motors – Theory and Applications*, Oxford University Press, New York, 1993.
- [2] K. Uchino, *Piezoelectric Actuators and Ultrasonic Motors*, Kluwer, New York, 1997.
- [3] K. Nakamura, M. Kurosawa, S. Ueha, Design of a hybrid transducer type ultrasonic motor, *IEEE Trans. Ultrason., Ferroelectr., Freq. Control* 40 (1993) 395–401.
- [4] K. Nakamura, S. Ueha, Potential ability of ultrasonic motors: a discussion focused on the friction control mechanism, *Electron. Commun. Jpn. Part 2* 81 (1998) 57–68.
- [5] W. Qiu, Y. Mizuno, D. Koyama, K. Nakamura, Efficiency improvement of hybrid transducer-type ultrasonic motor using lubricant, *IEEE Trans. Ultrason., Ferroelectr., Freq. Control* 60 (2013) 786–794.
- [6] H. Czichos, *Tribology – A System Approach to the Science and Technology of Friction, Lubrication and Wear*, Elsevier, New York, 1978.
- [7] W. Qiu, Y. Mizuno, M. Tabaru, K. Nakamura, Can lubricant enhance the torque of ultrasonic motors? An experimental investigation, *Appl. Phys. Lett.* 105 (2014) 4.
- [8] K. Adachi, K. Kato, Y. Sasatani, The micro-mechanism of friction drive with ultrasonic wave, *Wear* 194 (1996) 137–142.
- [9] T. Ishii, E. Matsuo, K. Nakamura, S. Ueha, K. Ohnishi, Characteristics of ultrasonic motors driven in a vacuum, *Jpn. J. Appl. Phys.* 37 (1998) 2956–2959.
- [10] T. Yamaguchi, K. Adachi, Y. Ishimine, K. Kato, Wear mode control of drive tip of ultrasonic motor for precision positioning, *Wear* 256 (2004) 145–152.
- [11] J. Olofsson, F. Lindberg, S. Johansson, S. Jacobson, On the role of tribofilm formation on the alumina drive components of an ultrasonic motor, *Wear* 267 (2009) 1295–1300.
- [12] J. Olofsson, S. Johansson, S. Jacobson, Influence from humidity on the alumina friction drive system of an ultrasonic motor, *Tribol. Int.* 42 (2009) 1467–1477.
- [13] A. Endo, N. Sasaki, Investigation of friction material for ultrasonic motor, *Jpn. J. Appl. Phys.* 26 (1987) 197–199.
- [14] P. Rabinovich, J. Wallaschek, Friction and wear behavior of polymer/steel and alumina/alumina under high-fretting conditions, *Wear* 216 (1998) 97–105.
- [15] J. Qu, Y. Zhang, X. Tian, W. Guo, Mechanical and tribological properties of eponol blends as frictional materials of ultrasonic motors, *Tribol. Lett.* 56 (2014) 387–395.
- [16] J. Wallaschek, Contact mechanics of piezoelectric ultrasonic motors, *Smart Mater. Struct.* 7 (1998) 369–381.
- [17] C. Zhao, *Ultrasonic Motors – Technologies and Applications*, Science Press; Springer-Verlag, Beijing; Berlin, Heidelberg, 2011.
- [18] L.C. Erickson, A. Blomberg, S. Hogmark, J. Bratthall, Tribological characterization of alumina and silicon carbide under lubricated sliding, *Tribol. Int.* 26 (1993) 83–92.
- [19] K. Nakamura, M. Kurosawa, H. Kurebayashi, S. Ueha, An estimation of load characteristics of an ultrasonic motor by measuring transient response, *IEEE Trans. Ultrason., Ferroelectr., Freq. Control* 38 (1991) 481–485.
- [20] M.K. Kurosawa, State-of-the-art surface acoustic wave linear motor and its future applications, *Ultrasonics* 38 (2000) 15–19.
- [21] S.M. Hsu, M.C. Shen, Ceramics wear maps, *Wear* 200 (1996) 154–175.
- [22] K. Adachi, K. Kato, N. Chen, Wear map of ceramics, *Wear* 203–204 (1997) 291–301.
- [23] X. Dong, S. Jahanmir, L.K. Ives, Wear transition diagram for silicon carbide, *Tribol. Int.* 28 (1995) 559–572.
- [24] Y. Kimura, K. Okada, Y. Enomoto, Sliding damage of silicon nitride in plane contact, *Wear* 133 (1989) 147–161.